

Vapor-Phase Hydrothermal Transformation of HTiOF₃ Intermediates into {001} Faceted Anatase Single-Crystalline Nanosheets

Porun Liu, Yun Wang, Haimin Zhang, Taicheng An, Huagui Yang, Zhiyong Tang, Weiping Cai, and Huijun Zhao*

For the first time, a facile, one-pot hydrofluoric acid vapor-phase hydrothermal (HF-VPH) method is demonstrated to directly grow single-crystalline anatase TiO₂ nanosheets with 98.2% of exposed {001} faceted surfaces on the Ti substrate via a distinctive two-stage formation mechanism. The first stage produces a new intermediate crystal (orthorhombic HTiOF₃) that is transformed into anatase TiO₂ nanosheets during the second stage. The findings reveal that the HF-VPH reaction environment is unique and differs remarkably from that of liquid-phase hydrothermal processes. The uniqueness of the HF-VPH conditions can be readily used to effectively control the nanostructure growth.

Dr. P. R. Liu, Dr. Y. Wang, Dr. H. M. Zhang,
Prof. H. J. Zhao
Centre for Clean Environment and Energy
Griffith School of Environment
Griffith University
Queensland 4222, Australia
E-mail: h.zhao@griffith.edu.au

Prof. T. C. An
State Key Laboratory of Organic Geochemistry
Guangdong Key Laboratory of Environmental
Resources Utilization and Protection
Guangzhou Institute of Geochemistry
Chinese Academy of Sciences
Guangzhou 510640, P.R. China

Prof. H. G. Yang
Key Laboratory for Ultrafine Materials of Ministry of Education
School of Materials Science and Engineering
East China University of Science and Technology
Shanghai 200237, P.R. China

Prof. Z. Y. Tang
National Centre for Nanoscience and Technology
Beijing 100190, P.R. China

Prof. W. P. Cai
Key Laboratory of Materials Physics
Hefei Key Laboratory of Nanomaterials and Nanotechnology
Institutes of Solid State Physics
Chinese Academy of Sciences
Hefei 230031, P.R. China

DOI: 10.1002/sml.201200971



1. Introduction

Nanostructured TiO₂ materials have become a class of important functional materials for many emerging research fields, especially environmental remediation, solar energy conversion, and solar fuel production.^[1] The performance of such materials has long been known to be dependent on their sizes, shapes, morphologies, structures, and crystal phases.^[2] However, a recent realization of performance dependent on their crystal facets has stimulated an enormous interest to develop anatase TiO₂ structures dominated by highly reactive crystal facets.^[3] In this regard, the anatase TiO₂ structures with surfaces dominated by {001} facets are the most studied because {001} facets possess high reactivity for a wide range of applications.^[4]

Fabrication of anatase TiO₂ crystals with a dominant {001} faceted surface is thermodynamically unfavorable due to the high surface energy status of {001} facets.^[3a,b] To obtain such a highly reactive surface, an effective means to markedly reduce the {001} surface energy is a necessity. For this, a recently demonstrated surface fluorination approach by Yang and co-workers has proven to be the most successful means to effectively reduce the {001} faceted anatase surface energy to a level lower than that of the {101} faceted surface—the commonly dominant crystal surface for hydrothermally synthesized anatase TiO₂.^[3c] These methods have now been widely employed to synthesize {001} faceted anatase TiO₂

structures.^[3d,4,5] Three categories of {001} facets dominated anatase TiO₂ have been reported. One is micrometer-sized anatase TiO₂ single crystals with different percentages of exposed {001} facets.^[3c,6] Although these materials consist of highly reactive {001} facets, their performances are often compromised by the significantly reduced surface area due to the large crystal sizes.^[3c,6] A category of structures with assembly of {001} faceted nanostructures on the surface of the microstructures was then developed to increase the percentage of exposed {001} facets and total surface areas.^[4e,f,5d,7] Anatase TiO₂ microspheres have been the most used microstructures for nanostructure assembly.^[4e,f,5d,7] Anatase nanosheets with nearly 100% exposed {001} facets have been successfully assembled on anatase TiO₂ microspheres.^[4e] Such a micro-nano assembly strategy is able to significantly improve the percentage of exposed {001} facets of the individual crystal, but the improvement on the total surface area is limited by the micrometer-sized substrates.^[4e,f,5d,7] In an attempt to further improve the surface area, a new category of {001} faceted anatase TiO₂ nanocrystals was developed.^[4c,8] The anatase TiO₂ nanosheet with 98.7% exposed {001} facets recently reported by Yang et al. is a typical successful example of such nanostructures.^[8] In fact, the nanosheet is the most suitable geometric structure to achieve a near 100% {001} faceted surface while providing a large surface area.^[8] It should be noted that until now, all reported hydrothermal methods for fabrication of {001} faceted anatase TiO₂ have been exclusively conducted by liquid-phase hydro/solvothermal methods.

On the mechanistic front, noticeable progress has been made to understand the {001} facet formation processes via the fluorination approach.^[3c,5c,9] A decisive effect of fluorination to reduce the {001} faceted surface energy has been categorically confirmed. The dissociative adsorption of molecular forms of HF, but not F⁻, has also been validated as an essential step of the fluorination at anatase TiO₂ surfaces.^[9b] That is, the surface fluorination could be largely promoted in the presence of molecular forms of HF.^[9b] Inspired by these insightful findings, and also considering the volatile nature of HF, we speculate that the vapor-phase hydrothermal (VPH) process could be superior to that of conventional liquid-phase hydrothermal (LPH) processes for the controlled growth of anatase TiO₂ with {001} facets dominating the surface. Under hydrothermal conditions in the presence of HF solution, the vapor phase will be saturated by the molecular forms of HF, the essential crystal facet control reagent. This differs remarkably from LPH processes in which the chemical forms and available concentrations of HF can be affected by many factors (e.g., the concentration, solution composition, and pH). Additionally, the formation mechanism under VPH conditions could also differ from that of LPH processes. We recently demonstrated that the size, morphology, and formation mechanism of the titanate nanotubes from an NH₃-VPH process are very different from those of conventional LPH processes.^[10] To the best of our knowledge, no VPH method has been reported for the fabrication of {001} faceted anatase TiO₂.

Herein, we report, for the first time, a facile hydrofluoric acid vapor-phase hydrothermal (HF-VPH) method to directly grow uniformly distributed single-crystalline anatase

nanosheets with 98.2% of exposed {001} facets on the Ti substrate. A systematic investigation was carried out to confirm the structure of the hydrogen titanium oxyfluoride intermediate, HTiOF₃, under the VPH conditions, and the nanosheet formation mechanism via hydrothermal transformation of the intermediate HTiOF₃ crystals. Experiments were also carried out to demonstrate a convenient way of controlling the dimensions and percentage of exposed {001} facets of the nanosheets. The photoelectrocatalytic activities of the resultant nanosheets were evaluated using glucose as the probe material.

2. Results and Discussion

2.1. Nanosheet Growth

The synthesis of the anatase nanosheet was performed in a heated Teflon-lined autoclave with a Ti foil located above diluted HF solution (Supporting Information, Figure S1). The structure, morphology, crystal phase, and exposed crystal facets of the as-synthesized samples after 3.0 h of HF-VPH treatment at 230 °C were firstly investigated. A pure anatase TiO₂ crystal phase^[11] (space group *I41/amd*, JCPDS No. 21-1272) was confirmed by the X-ray diffraction (XRD) data obtained from the as-synthesized product (**Figure 1a**). The Ti substrate was found to be uniformly covered by ultrathin anatase TiO₂ sheets (**Figure 1b**). These sheets exhibit nanometer-sized thickness and micrometer-sized width and length. A statistical analysis of scanning electron microscopy (SEM) data reveals that the microsized dimensions of these nanosheets is fairly uniform, with an average size of ≈1.76 μm (see below for details). A typical transmission electron microscopy (TEM) image of the nanosheets is shown in **Figure 1c**. This ultrathin individual nanosheet is almost

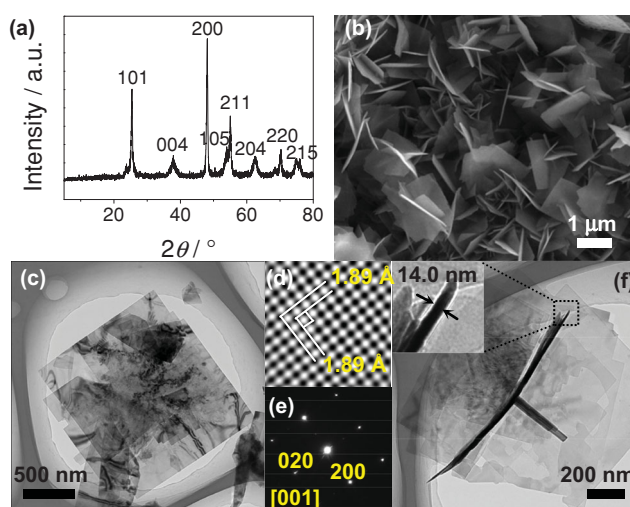


Figure 1. Structural properties of the as-synthesized anatase nanosheets subjected to HF-VPH treatment for 3.0 h at 230 °C. a) XRD data, b) SEM image, c) TEM image, d) HRTEM image with the incident beam normal to a nanosheet, e) SAED pattern, and f) TEM image showing the thickness of a nanosheet.

transparent under the electron-beam illumination. The high-resolution TEM (HRTEM) image with the incident beam normal to an anatase nanosheet demonstrates well-resolved (020) and (200) atomic planes, with an identical interspacing of 1.89 Å (Figure 1d). The corresponding selected-area electron diffraction (SAED) pattern can be indexed as the diffraction spots of the [001] zone of an anatase single crystal (Figure 1e).^[3c] These results confirm that the as-synthesized anatase nanosheets are enclosed with high-quality {001} faceted surfaces. A side-view TEM image exhibits a nanosheet thickness of 14.0 nm (Figure 1f), which is approximately the size of 15 unit cells. A detailed statistical analysis reveals that 92.8% of the as-synthesized nanosheets possess a thickness within the 13.0–16.0 nm range (see below for details). An average percentage of 98.2% of exposed {001} facets was thus obtained according to the anatase crystallographic structure^[11] and the statistically measured nanosheet dimensions.

SEM and XRD analyses of the as-synthesized products at different stages of the reaction were performed to investigate the nanosheet formation processes (Figure 2). A dense layer of particulate products having particle sizes between 300 and 500 nm were formed on the Ti substrate within 30 min of HF-VPH treatment (Figure 2a). The formed particulate products evolved into larger ($\approx 1 \mu\text{m}$), well-defined hexagonal-shaped crystals after 1.5 h of HF-VPH treatment (Figure 2b). These well-defined hexagonal crystals were identified to be a new form of intermediate crystal (later identified as HTiOF₃). The clearly visible sheetlike structures started to form on the surface of the hexagonal-shaped HTiOF₃ crystals when the sample was treated by HF-VPH for 2.0 h; note that the size of the HTiOF₃ crystals was further increased to $\approx 2 \mu\text{m}$ (Figure 2c). Figure 2d shows the SEM image obtained from a sample after 2.5 h of HF-VPH treatment. An increased population of the sheetlike structures was observed, with the disappearance of the hexagonal-shaped HTiOF₃ crystals. The observed large-sized irregular-shaped particles are likely to be the remains of the hexagonal-shaped HTiOF₃ crystals, which suggests that the dissolution of the HTiOF₃ crystals might occur. This could also imply that the HTiOF₃ crystals served as a type of intermediate and their dissolution products were the building materials to form the nanosheets. This is supported by the SEM image obtained from the sample subjected to 2.8 h of HF-VPH treatment, for which the entire substrate was covered by densely populated pure nanosheets without a trace of the irregular-shaped particles (Figure 2e). When the reaction time was increased to 3.5 h, the nanosheet structures were eroded due to selective etching on the {001} faceted surfaces (Figure 2f).^[9b]

Figure 2g shows the XRD data of the as-synthesized products from different reaction times. The XRD pattern obtained from a sample treated for 0.5 h was dominated by the Ti diffraction peaks, which weakened as the HF-VPH treatment time increased. The XRD patterns obtained from the well-defined hexagonal-shaped crystals (HF-VPH treated for 1.5 and 2.0 h) exhibit a group of diffraction peaks (belonging to HTiOF₃, see below for details) that are similar to those obtained from ammonium oxo-fluorotitanate, NH₄TiOF₃.^[12] The XRD pattern obtained from the sample containing nanosheets and small numbers of large, irregular-shaped

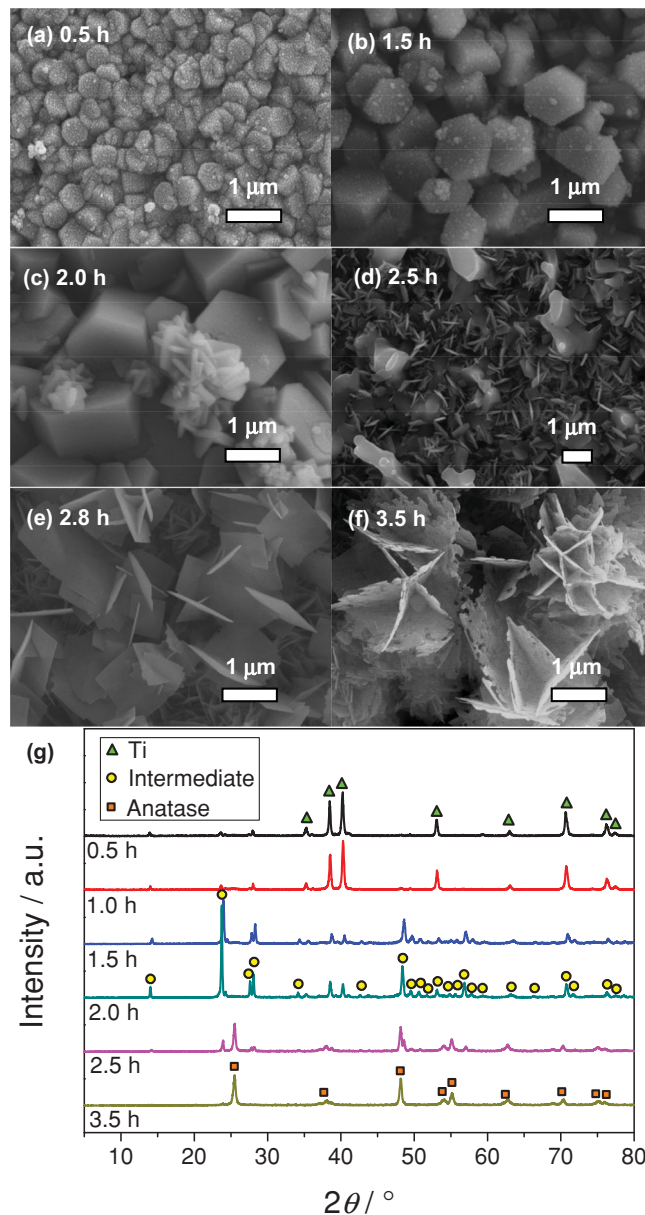


Figure 2. a–f) SEM images and g) XRD patterns of the as-synthesized samples subjected to HF-VPH treatments for 0.5–3.5 h at 230 °C.

particles (with 2.5 h treatment) was dominated by the diffraction peaks of anatase TiO₂, while the peaks belonging to the hexagonal-shaped HTiOF₃ crystals were significantly weakened. This finding confirms that the irregular-shaped particles are indeed the remains of the hexagonal-shaped HTiOF₃ crystals. The XRD pattern obtained from the sample containing pure nanosheets (with 3.0 h of treatment) can be indexed to pure anatase TiO₂ crystals (Figure 1a). These XRD data correspond perfectly to the structural changes observed in the SEM images, thus suggesting a two-stage formation process.

The first-stage structural formation process (within 0–1.5 h of treatment) involves the dissolution of Ti to form the hexagonal-shaped HTiOF₃ intermediate crystals. The second-stage structural formation process (within 1.5–3.0 h of treatment) starts after the HTiOF₃ intermediate crystals

reach their maturity. This involves the rapid dissolution of HTiOF₃ intermediate crystals that is accompanied by a speedy nanosheet growth process. In fact, during this stage of the reaction, the HTiOF₃ intermediate crystals are hydrothermally transformed into anatase nanosheets. However, a detailed transformation process cannot be given until the structural and compositional characteristics of HTiOF₃ are precisely identified.

2.2. Characteristics of Intermediates

The formation and transformation of the hexagonal-shaped intermediate are crucial for the growth of the nanosheets. Therefore, precise structural and compositional information of the intermediate is critically important for obtaining insightful mechanistic pathways of nanosheet formation. As mentioned above, the XRD patterns obtained from the well-defined hexagonal-shaped intermediate crystals are very similar to those obtained from NH₄TiOF₃. However, the structure of the intermediate crystals obtained in this work should be different from that of NH₄TiOF₃, considering the absence of ammonium species in our synthesis process. Other techniques were therefore employed to examine the structural characteristics of the intermediate crystals. Energy-dispersive X-ray spectroscopy (EDXS) and X-ray photoelectron spectroscopy (XPS) were employed to determine the elemental composition of the intermediate crystals. The EDXS data shown in Figure S2 confirm the presence of O, F, and Ti elements. This was further confirmed by the XPS data shown in **Figure 3a**. The high-resolution XPS spectra of F 1s core electrons obtained from the intermediate crystals reveal a symmetric peak centered at 684.5 eV, attributable to the oxofluorotitanate type of Ti–F species (Figure 3b).^[13] The atomic percentage of the F species found from the intermediate was 13.4%, which is nearly double the content

found from the anatase TiO₂ nanosheet. The presence of F in the anatase TiO₂ nanosheet can be attributed to the surface-absorbed Ti–F species.^[3c,14] The O 1s spectra of both the anatase nanosheet and intermediate (Figure 3c) are asymmetric and can be attributed to two different types of O atoms. The major contribution is the lattice oxygen (Ti2O) centered at 530.1 eV and the minor contribution at 531.5 eV can be ascribed to hydroxyl groups or absorbed water on the surface.^[15] Moreover, the oxidation state of Ti species in both the anatase nanosheet and intermediate crystals centered at 464.6 and 458.9 eV (a spin–orbit splitting of 5.7 eV) can be assigned to the 2p_{1/2} and 2p_{3/2} core levels of Ti^{IV}.^[15a,16]

Figure 4a shows the Raman spectra of samples subjected to 1.5 and 3.0 h of HF–VPH treatment. Three major peaks at 207.8, 442.3, and 602.1 cm⁻¹ were observed from a sample consisting of pure hexagonal-shaped intermediate crystals (with 1.5 h of treatment), which can be assigned to the ν₆, ν₂, and ν₁ modes of a fluorotitanate.^[17] This strongly suggests that the intermediate framework is composed of TiO_xF_y octahedra. Also, no band at about 650.0, 530.0, or 439.0 cm⁻¹

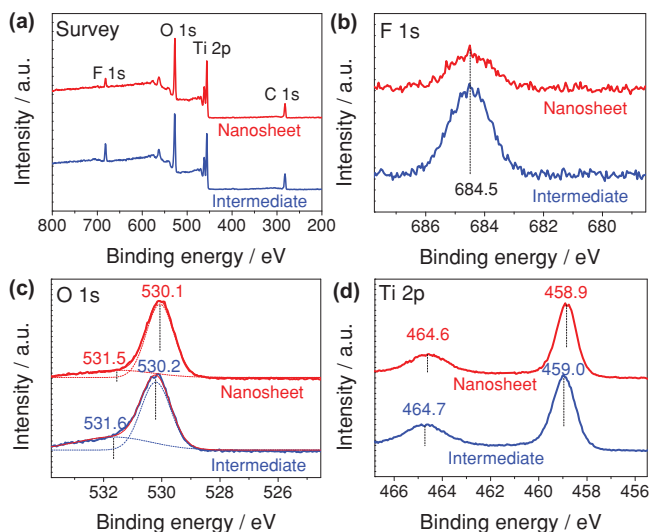


Figure 3. XPS spectra of the intermediate (1.5 h sample) and TiO₂ nanosheets (3.0 h sample): a) Survey scans, b) F 1s peaks, c) O 1s peaks, and d) Ti 2p peaks.

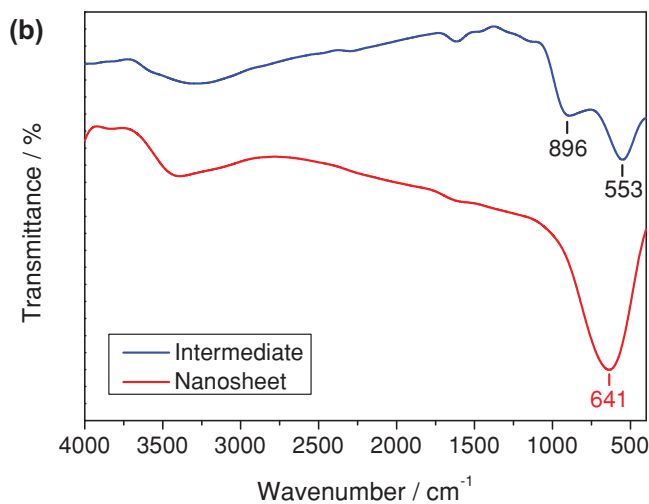
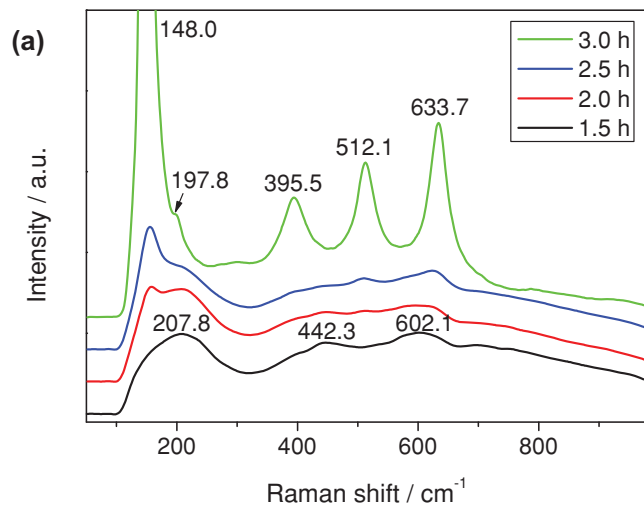


Figure 4. a) Raman spectra of samples subjected to 1.5–3.0 h of HF–VPH treatment. b) IR spectra of the intermediate (1.5 h sample) and anatase TiO₂ nanosheets (3.0 h sample).

is detected, thus indicating that the intermediate is free of Ti–O–Ti bonds.^[18] The data obtained from an intermediate crystal dominated sample with a low nanosheet content (with 2.0 h of treatment) revealed a new peak at 148.0 cm⁻¹ with a noticeable weakening of the fluorotitanate peaks. When the nanosheet content of a sample was increased (with 2.5 h of treatment), an increased intensity of the peak at 148.0 cm⁻¹ was observed. This was accompanied by decreased intensities of the fluorotitanate peaks. For a sample consisting of pure anatase TiO₂ nanosheets without the presence of the intermediate crystals (3.0 h HF-VPH treated sample), the Raman spectrum displays a set of typical energy bands of anatase TiO₂ phase at 148.0 (*E_g*), 197.8 (*B_{1g}*), 395.5 (*A_{1g}*), 512.1 (*B_{1g}*), and 633.7 cm⁻¹ (*E_g*).^[19] These results correspond well with the observed morphological and crystal-phase changes demonstrated by the SEM and XRD data.

Figure 4b shows the Fourier transform infrared (FTIR) spectra of the anatase TiO₂ nanosheets (with 3.0 h of treatment) and the intermediate crystals (with 1.5 h of treatment), which correspond to the samples shown in Figures 1b and 2b. It was found that for the sample containing pure anatase TiO₂ nanosheets (bottom red line), only one intensive band centered at 641.6 cm⁻¹ and originating from the Ti–O–Ti vibrations was recorded.^[20] For the intermediate (top blue line), two bands at 896.4 and 553.3 cm⁻¹ were recorded, attributable to the $\nu(\text{Ti}-\text{O}_t)$ mode (O_t is terminal oxygen) and $\nu(\text{Ti}-\text{F})$ mode of the oxofluorotitanate (TiOF_3^-), respectively.^[12a] It has been revealed that the band position resulting from the Ti–F stretching vibration varies depending on the structural arrangement of the octahedral TiO_xF_y structures (i.e., isolated, chainlike, or layers).^[12a] In our study, the 553.3 cm⁻¹ band obtained from the intermediate is found to be close to the $\nu(\text{Ti}-\text{F})$ mode of layered NH_4TiOF_3 .^[12a] This suggests that the intermediate might be constructed from layered TiO_xF_y octahedral structures. Also, in good agreement with the Raman spectra, the absence of the $\nu(-\text{Ti}-\text{O}-\text{Ti}-)$ mode and the presence of the $\nu(\text{Ti}-\text{O}_t)$ mode in the IR spectra of the intermediate suggest that the oxygen atoms in the intermediate are located above the Ti–F network plane level rather than in the bridging positions.^[12a] To date, TiOF_2 has been the only identified intermediate for the formation of single-crystalline anatase TiO₂ under LPH conditions in the presence of F species.^[8,21] All experimental evidence obtained by us so far demonstrates that the structural characteristics of the intermediate obtained in this work under HF-VPH conditions are remarkably different from those reported for TiOF_2 under LPH conditions.^[8,21] Therefore, it can be concluded that the intermediate obtained from the HF-VPH process is a new intermediate.

The compositional and structural characteristics confirmed by the above experimental evidence strongly allude to the fact that the atomic structure of the obtained intermediate could be a type of oxofluorotitanate species. To confirm the exact structure of the intermediate, a total of 40 possible configurations of the oxofluorotitanate species were established based on the structural characteristics and were systematically evaluated using density functional calculations. A hydrogen oxofluorotitanate crystal, HTiOF₃ (Figure 5a,d,g; orthorhombic, $a = b = 3.75$, $c = 12.59$ Å), was found to be the

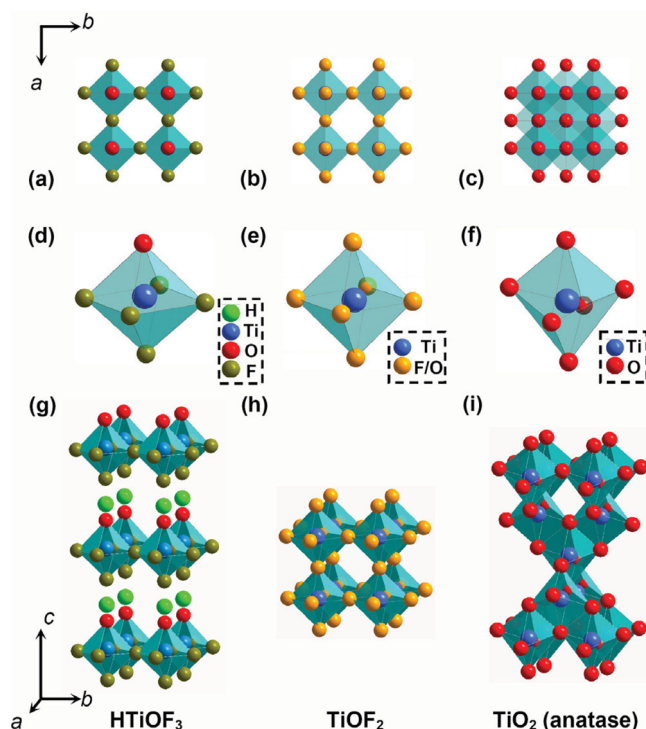


Figure 5. Schematic diagrams of HTiOF₃, TiOF₂, and anatase TiO₂ crystal structures. a–c) Projection viewed along the [001] direction; d–f) single TiO_xF_y octahedral building block; g–i) unit cell.

most stable crystal structure among all considered configurations. For comparison, the structures of TiOF₂ and anatase are also shown in Figure 5. In strong contrast to the other two structures, the HTiOF₃ crystal has a layered structure composed of corner-shared TiO₅F octahedra while the neighboring layers are separated by hydrogen atoms. Individual TiO₅F octahedra at the same layers are connected with each other by sharing four corner F atoms. The layers are stacked along the *c* axis via hydrogen bonds. Unlike the TiOF₂, there is no Ti–O–Ti bond in the HTiOF₃ crystal structure and the oxygen atoms locate at the terminal corners of TiO₅F octahedra on one side of the layer level, which is in agreement with the data from Raman and FTIR spectroscopy. Our results also show that the alternatively located oxygen atoms, for example at the bridging positions, will possess a total energy approximately 30 kJ mol⁻¹ higher than that of the most stable configuration.

To validate the theoretically calculated HTiOF₃ structure, an XRD pattern was simulated based on the optimized HTiOF₃ structure (Figure 6; Table S1, Supporting Information). All simulated diffraction peaks of HTiOF₃ were found to almost perfectly match the experimentally measured XRD pattern of the intermediate. This was further validated by HRTEM and SAED of HTiOF₃ crystals obtained by the incident beams along two different directions. Figure 7 presents a TEM image of a well-defined HTiOF₃ crystal with a width of ≈1 μm. The HRTEM image (Figure 7b) exhibits two crystal planes with equal spacing distances of 3.75 Å. The interfacial angle is 90.0°. These data are consistent with the theoretical values of the HTiOF₃ crystal (Table S1) for the (100) and

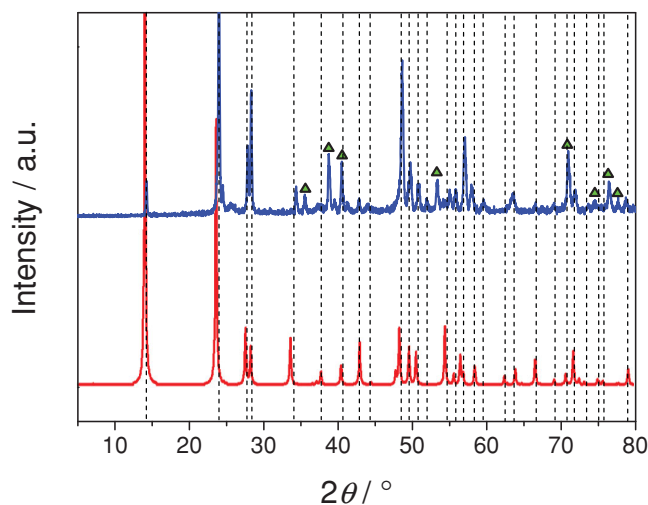


Figure 6. Comparison of the experimentally measured XRD data (top blue line) and simulation results (bottom red line) of intermediate HTiOF₃. Peaks marked with empty triangles: Ti substrate.

(010) planes and the interfacial angle. The corresponding SAED pattern (Figure 7c) reveals that the examined crystal is a single crystal and the pattern can be indexed to the (*hk*0) reflections with the [001] zone axis. Likewise, a set of data (Figure 7d–f) was acquired with a different crystal in the same TEM sample. The plane spacing and interfacial angle are measured as 3.75 Å, 6.30 Å, and 90.0°, which are in good agreement with the theoretical values for the (100) and (002) planes of the HTiOF₃ crystal. The SAED pattern (Figure 7f) can be assigned to the crystal along the [010] direction. These results confirm that the obtained intermediate crystal is the orthorhombic HTiOF₃ crystal.

2.3. Formation Mechanism

The above experimental evidence demonstrates a distinctive two-stage structural formation process. The first stage of the HF-VPH process (0–1.5 h) produces the HTiOF₃

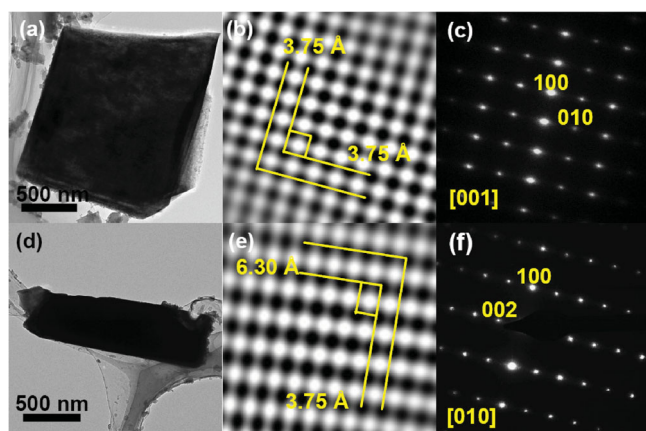


Figure 7. TEM and HRTEM images and SAED patterns of the HTiOF₃ crystals (1.5 h sample) with the incident beam along the a–c) <001> and d–f) <010> directions.

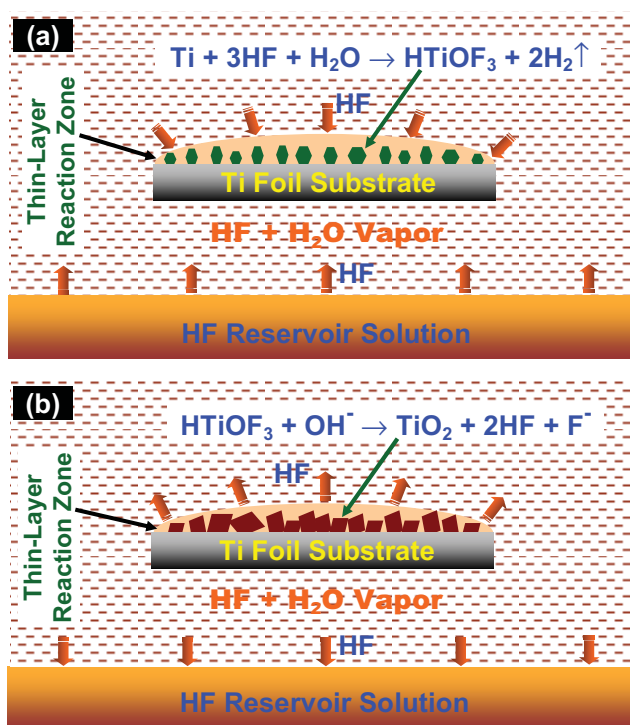
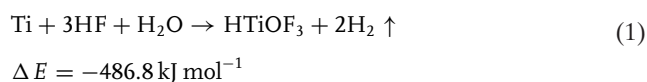


Figure 8. Schematic illustration of the two-stage HF-VPH process. a) First stage of the process to produce HTiOF₃ intermediate crystals, and b) second stage of the process to transform the intermediate crystals into anatase TiO₂ nanosheets.

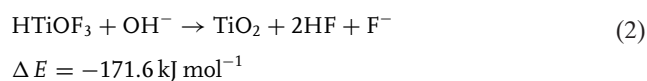
intermediates that are transformed to the anatase TiO₂ nanosheets during the second stage of the HF-VPH process (>1.5 h). Such a distinctive two-stage structural formation process can be attributed to the unique reaction environment created under the HF-VPH conditions. For a conventional LPH system, all reactions take place in the bulk solution (the reaction medium). The titanium species from the dissolution of the titanium substrate diffuse into the bulk solution and the structure formation can occur only after the concentration of the dissolved titanium species in the reaction medium reaches saturation status. In contrast, a HF-VPH system consists of a reactant reservoir (e.g., HF solution as shown in Figure S1 and Figure 8). All reactions occur within a thin-layer reaction zone formed on the surface of the substrate by the condensation of HF-saturated water vapor (Figure 8). Importantly, the reactant concentration in the thin-layer reaction zone (the reaction medium) depends on the partial pressure (*P_i*) of the volatile reactant in the vapor phase (e.g., HF), the reactant concentration in the reservoir solution, and the rate of reactant consumption in the reaction zone. This means that the reactant concentration in the thin-layer reaction zone is determined by the dynamic equilibrium of the volatile reactant (e.g., HF) at the thin-layer reaction liquid/vapor/reservoir liquid interfaces. These dynamic equilibria at the two liquid/vapor interfaces are linked by the *P_i* of the volatile reactant. For this work, the direction of the dynamic equilibrium shift is driven by the consumption/release of HF in the thin-layer reaction zone (Figure 8).

The formation of HTiOF₃ intermediate during the first stage of the HF-VPH process could be attributed to the HF-rich reaction environment created under the HF-VPH conditions (Figure 8a). An HF-rich thin-liquid-layer reaction zone on the substrate surface is instantly formed at the beginning of the HF-VPH process resulting from the condensation of HF-saturated water vapor. The high concentration of HF within the thin-liquid-layer reaction zone can be attributed to rapid HF transport in the vapor phase and the short diffusion distance within the thin-liquid-layer reaction zone. The high HF concentration leads to a rapid dissolution of Ti substrate. Under such conditions, the calculation result indicates that the formation of HTiOF₃ intermediate [Eq. (1)] is thermodynamically favorable having an overall reaction energy of $-486.8 \text{ kJ mol}^{-1}$.



The dissolution product of HTiOF₃ rapidly supersaturates the thin-liquid-layer reaction zone due to the small volume, thereby leading to precipitation to form the HTiOF₃ crystal structures. This process continues while the reservoir solution can supply sufficient HF (maintaining a sufficiently high HF vapor pressure) via evaporation. It is important to note that the formation of HTiOF₃ increases the pH of the thin-liquid-layer reaction zone, thus leading to a lower effective HF concentration in the reaction zone. Also, the evaporation of HF increases the pH of the reservoir solution, which leads to a decreased HF partial pressure in the vapor phase. The supply of HF will gradually slow down as the reaction progresses due to the increased pH (cause by evaporation) and decreased HF concentration (consumed by the reaction) in the reservoir solution. As such, the system eventually reaches a critical point at which the HF concentration in the reaction zone is insufficient to dissolve the Ti substrate. The structure formation of HTiOF₃ is therefore stopped, which marks the end of the first stage of the HF-VPH process.

As shown in Figure 5a and g, viewing from the [001] direction, the HTiOF₃ can be considered as a layer-structured crystal composed of corner-shared TiO_xF_y octahedral units separated by a hydrogen layer. The calculation confirms that the interlayer connection of the HTiOF₃ crystal is through the relatively weak hydrogen bonds. The relatively high pH in the reaction zone at the end of the first stage of the HF-VPH process destabilizes the interlayer hydrogen bonds, thereby triggering the dissolution of HTiOF₃ to form anatase TiO₂ [Eq. (2)], which marks the beginning of the second stage of the HF-VPH process (Figure 8b).



The calculation result indicates that the transformation of HTiOF₃ intermediates into TiO₂ is thermodynamically permitted, with an overall reaction energy of $-171.6 \text{ kJ mol}^{-1}$. Under the HF-VPH conditions, the precipitation of TiO₂ is highly localized due to the limited mass-transport capability

of the thin liquid layer along the direction of the substrate surface. The released HF serves as the crystal-facet-directing reagent to stabilize the {001} facets.^[3c] Under such conditions, the growth of anatase TiO₂ along the directions normal to the [001] direction leads to the formation of the {001} facet dominated nanosheet. It should be noted that the release of HF during the second stage of the HF-VPH process [Eq. (2)] decreases the pH and increases the effective HF concentration in the thin-liquid-layer reaction zone. This leads to a selective etching on the {001} faceted surfaces with prolonged reaction time^[9b] (Figure 2f), although the excess HF can be released to the vapor phase and adsorbed by the reservoir solution (Figure 8b).

Further experiments were performed to confirm the role of HF as the crystal facet-directing reagent. The sample after 1.5 h of HF-VPH treatment was removed from the reactor. The formed HTiOF₃ intermediate crystals were then subjected to a VPH treatment with pure water as the reservoir solution in the absence of HF. The SEM and TEM images and XRD data obtained from the resultant sample (Figure S3) confirm that without the surface fluorination, the HTiOF₃ intermediate crystals were transformed into spherical-shaped anatase TiO₂ crystals with {101} exposed crystal facets.

2.4. Growth Control

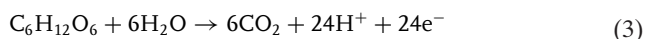
Mechanistic studies have confirmed the decisive role of molecular forms of HF for the formation of {001} faceted anatase TiO₂.^[3c,9a,b] We have recently demonstrated that for a given total fluoride concentration under LPH conditions, a change in solution pH can lead to dramatic changes in size, shape, morphology, and percentage of exposed {001} facets of the anatase TiO₂ crystals.^[9a] In effect, a change in pH under such circumstances changes the concentration of the molecular forms of HF.^[9a] This might mean that the controlled growth of anatase TiO₂ crystals with different sizes and percentages of exposed {001} facets can be achieved by controlling the concentration of the molecular forms of HF. With the HF-VPH method, the control of the vapor-phase HF concentration or partial pressure of the molecular forms of HF can be readily achieved by controlling the reaction temperature. A higher reaction temperature will lead to a higher HF partial pressure/concentration in the vapor phase. Figure S4a,d,g shows the anatase TiO₂ nanosheets with different dimensions and percentages of exposed {001} facets obtained from HF-VPH processes under the controlled temperatures of 180, 200, and 230 °C, respectively.

As expected, an increase in the reaction temperature leads to an increase in the percentage of {001} faceted surfaces of the resultant nanosheets. Approximately 83.9, 93.0, and 98.2% of exposed {001} faceted surfaces were obtained when the treatment temperature was increased from 180 to 200 and 230 °C, respectively (Figure S4). It was found that an increased reaction temperature results in an increase in the micro dimensions (widths) but a decrease in the nano dimension (thickness) of the nanosheets. At 180 °C, the measured widths and thickness of the nanosheets were found to be between 0.80 and 0.90 μm (with an average width of $\approx 0.86 \mu\text{m}$)

and 65.0–84.0 nm (with an average thickness of ≈ 72.9 nm), respectively. The statistical results showed that approximately 90.2% of nanosheets prepared under such conditions had a thickness between 68.0 and 80.0 nm. For nanosheets prepared at 200 °C, the widths and thicknesses were distributed within the range of 1.10–1.45 μm (with an average width of ≈ 1.29 μm) and 37.0–49.0 nm (with an average thickness of ≈ 43.9 nm), respectively; 90.3% of the nanosheets had thicknesses between 38.0 and 48.0 nm. With the reaction temperature of 230 °C, the widths of the nanosheets were further increased to 1.45–2.00 μm (with an average width of ≈ 1.76 μm) while the thicknesses were reduced to 13.0–17.0 nm (with an average thickness of ≈ 14.9 nm). The majority (92.8%) of the nanosheets had a thickness within 13.0–16.0 nm. The above results demonstrated that with the HF-VPH method, the dimensions and percentage of exposed {001} facets can be readily controlled by controlling the reaction temperature.

2.5. Photocatalytic Activity

The resultant anatase nanosheets with different percentages of exposed {001} facets were used as photoanodes to evaluate their photoelectrocatalytic activities (Figure S5). Glucose was selected as the test compound. The complete mineralization of glucose can be presented as:



Such a photocatalytic degradation process is essentially an electron-transfer process.^[22] The measured photocurrent under suitable conditions represents the incident rate of electron transfer that can be the best to represent the rate of photocatalytic degradation, and hence the photocatalytic activity of the photoanode.^[23] However, the photocurrent can be used to evaluate the photoactivity only when 100% of photoelectrons originating from photocatalytic oxidation of glucose are collected.^[22] In this work, our experimental results suggested that such a 100% collection efficiency of photoelectrons can be achieved by application of a +0.80 V potential bias. Figure S5a–c shows the photocurrent profiles of the three photoanodes under a constant potential bias of +0.80 V. The blank photocurrent (i_{blank}) was obtained from the solution containing 0.1 M NaNO_3 electrolyte without glucose. For all cases, a photocurrent spike was observed initially and then reached a steady state within 10 to 30 s. The initial photocurrent spike can be attributed to the preabsorbed electroactive species (e.g., water and glucose in our case) on the photoanode surface before the UV illumination.^[22a,b,d] With a working solution containing different concentrations of glucose, it was found that an increase in the glucose concentration resulted in an increase in the overall photocurrent (i_{total}). It should be noted that i_{total} consists of two components: one from the photocatalytic oxidation of water, which is essentially constant for a given photoanode under a fixed light intensity, and the other from the photocatalytic oxidation of glucose.^[22a,b,d] The net photocurrent (i_{net}) originating from the photocatalytic oxidation of glucose can be obtained by subtracting the i_{blank} from the i_{total} ($i_{\text{net}} = i_{\text{total}} - i_{\text{blank}}$).^[22a,b,d]

Under the experimental conditions employed, the measured i_{net} value represents the rate of photocatalytic oxidation of glucose at the photoanode.^[22a,b,d] Figure S5d shows the net photocurrent density ($J_{\text{net}} = i_{\text{net}}/\text{exposed surface area of the photoanode}$) plotted against the glucose concentration. Linear relationships between the measured J_{net} and the glucose concentrations were obtained from all three photoanodes studied. The slopes of the $J_{\text{net}}-C$ curves were measured to be 618.41 ($R^2 = 0.9914$), 492.41 ($R^2 = 0.9978$), and 442.85 $\mu\text{A cm}^{-2} \text{mM}^{-1}$ ($R^2 = 0.9990$) for the photoanodes prepared at 230, 200, and 180 °C, respectively. These slope values are the quantitative representation of the photocatalytic activities of the photoanodes investigated.^[22a,b,23] These results suggest that the photocatalytic activity of the photoanode with 98.2% of exposed {001} facets is approximately 1.26 and 1.40 times that of the photoanodes with 93.0 and 83.9% of exposed {001} facets, respectively. Given that all photoanodes were coated with a similar amount of anatase nanosheets, it should be reasonable to attribute the enhanced photoactivity to the increased percentage of {001} faceted surface. Similar claims have also been made by other researchers.^[4]

3. Conclusion

We have successfully demonstrated, for the first time, a facile, one-pot HF-VPH method for direct growth of single-crystalline anatase TiO_2 nanosheets with nearly 100% of highly active {001} facets. We have revealed a distinctive two-stage formation mechanism. Precise structural information for the HTiOF_3 intermediate crystals has been provided, and the transformation of the intermediate crystals into single-crystalline anatase TiO_2 nanosheets has been evidenced. We have also demonstrated that the controlled growth of single-crystalline anatase TiO_2 nanosheets with different sizes and percentage of exposed {001} facets can be readily achieved by controlling the reaction temperature, and the photocatalytic activities are closely related to the percentage of exposed {001} facets. More importantly, the findings of this work reveal that the reaction environment created under HF-VPH conditions is unique and differs remarkably from that of conventional LPH processes. This is highly significant as such a unique reaction environment can be utilized to obtain new forms of materials via different formation mechanisms. The reported VPH method could be a general method that is applicable to other metal oxide systems.

4. Experimental Section

Materials: Hydrofluoric acid (HF, 48%, Aldrich) and glucose (AR, Aldrich) were used as received. All aqueous solutions were prepared using high-purity water (Millipore Corp., 18 M Ω cm). Titanium metal plates (0.25 mm, 99.7%, Aldrich) and indium tin oxide (ITO) conducting glass slides (Delta Technologies Ltd., 8 Ω square⁻¹) were washed in acetone and water under ultrasonic conditions and dried in a nitrogen stream before use.

Synthesis: All HF-VPH fabrication experiments were carried out in a water/HF mixed vapor environment in a sealed Teflon-lined autoclave (Figure S1).^[10] The autoclave contained HF solution

(2.2%, 5 mL) to generate water/HF mixed vapor at elevated temperatures of 180–230 °C. A Teflon holder was used to hold the Ti plates (16 × 20 × 0.25 mm) about 3 cm above the HF solution. After synthesis (0.5–6.0 h), the autoclave was placed in a fume cupboard for cooling. The Ti plates coated with the as-prepared products were rinsed with water (50 mL) three times to remove the excess HF acid and dried at room temperature ready for further characterization or photocatalysis experiments. The production capacity could be readily scaled up by placing multiple Ti metal substrates above the HF solution providing that the amount of the reservoir solution was sufficient.

Characterization: Morphological properties of the as-prepared samples were investigated by a JSM-6300 scanning electron microscope. EDXS was conducted with an XL-30 SEM instrument. The microstructure was examined by field-emission TEM (Tecnai F20) with an accelerating voltage of 200 kV. XRD data were collected with a Bruker X-ray diffractometer equipped with a graphite monochromatic copper radiation ($\text{Cu K}\alpha$) system operated at 40 kV and 30 mA. Raman spectra were collected with a Renishaw 100 system Raman spectrometer using a 632.8 nm He–Ne laser. The scattered light was detected with a Peltier-cooled CCD detector with spectral resolution of 2.0 cm^{-1} . The grating was calibrated using the 520.0 cm^{-1} silicon band. FTIR spectra were collected with a Perkin–Elmer Spectrum 1000 FTIR spectrometer. The XPS data were acquired using a Kratos Analytical Axis Ultra X-ray photoelectron spectrometer equipped with a monochromatic Al X-ray source (Al $\text{K}\alpha$, 1.487 keV). The C 1s was used as the charge reference with a binding energy of 284.8 eV.

Computation: All computations were performed using the Vienna ab initio simulation package (VASP) based on the all-electron projected augmented wave (PAW) method.^[24] A plane-wave basis set was employed to expand the smooth part of wave functions with a kinetic energy cutoff of 500 eV. For the electron–electron exchange and correlation interactions, the Perdew and Wang functional (PW91),^[25] a form of the general gradient approximation (GGA), was used throughout. Brillouin-zone integrations were performed using Monkhorst–Pack grids of special points, with gamma-point centered ($8 \times 8 \times 2$) k -point meshes used for the bulk cells. When the geometry was optimized, all atoms were allowed to relax. The geometric structure was optimized until the residual forces were below 0.001 eV \AA^{-1} .

Photoelectrocatalysis: The anatase nanosheet photoanodes were prepared by coating a nanosheet layer onto an ITO glass slide. Typically, the anatase nanosheet sample (0.01 g) was dispersed in ethanol solution (6.0 mL) in an ice bath with a Branson Sonifier ultrasonic homogenizer (with 50% amplitude) for 10 min with a 50 s flash and 10 s interval. The anatase nanosheets were coated onto the ITO slide by vertically withdrawing it from the above solution at a speed of 2 mm s^{-1} (repeated twice). After drying at room temperature, the photoanodes were calcined at 450 °C for 1 h. The photoelectrocatalytic oxidation of glucose was carried out in a photoelectrochemical cell consisting of a three-electrode electrochemical system.^[22b,26] The nanosheet-coated photoanode, a saturated Ag/AgCl electrode, and a platinum mesh were used as the working, reference, and counter electrodes, respectively. A voltammogram (CV-27, BAS) was used for application of potential bias. Potential and current signals were recorded using a Macintosh computer coupled to a MacLab 400 interface (AD Instruments). A 150 W xenon arc lamp with light filter (UG 5, Avotronics Pty. Ltd.)

was used as UV light source. The UV light intensities were set at 7.0 mW cm^{-2} (measured by a UV-irradiance meter, Beijing Normal University). The area of the UV illumination was 0.78 cm^2 . The steady-state photocurrent was measured with a bias potential of +0.80 V (vs. Ag/AgCl). The photocurrent measured at this potential represented the saturated photocurrent of the photoanode.^[22a,b] All photoelectrocatalysis experiments were conducted in a photoelectrochemical cell containing NaNO_3 (0.10 M) supporting electrolyte and glucose (0–0.05 mM).

Supporting Information

Supporting Information is available from the Wiley Online Library or from the author.

Acknowledgements

This work was financially supported by the Australian Research Council.

- a) A. J. Nozik, *Nature* **1975**, *257*, 383–386; b) A. Fujishima, K. Honda, *Nature* **1972**, *238*, 37–38; c) M. Fujihira, Y. Satoh, T. Osa, *Nature* **1981**, *293*, 206–208; d) S. U. M. Khan, M. Al-Shahry, W. B. Ingler, *Science* **2002**, *297*, 2243–2245; e) M. Gratzel, *Nature* **2001**, *414*, 338–344; f) U. Bach, D. Lupo, P. Comte, J. E. Moser, F. Weissortel, J. Salbeck, H. Spreitzer, M. Gratzel, *Nature* **1998**, *395*, 583–585.
- a) K.-S. Choi, *J. Phys. Chem. Lett.* **2010**, *1*, 2244–2250; b) Y.-w. Jun, J.-s. Choi, J. Cheon, *Angew. Chem. Int. Ed.* **2006**, *45*, 3414–3439; c) N. Murakami, Y. Kurihara, T. Tsubota, T. Ohno, *J. Phys. Chem. C* **2009**, *113*, 3062–3069; d) Y.-w. Jun, M. F. Casula, J.-H. Sim, S. Y. Kim, J. Cheon, A. P. Alivisatos, *J. Am. Chem. Soc.* **2003**, *125*, 15981–15985; e) Z. Zhang, X. Zhong, S. Liu, D. Li, M. Han, *Angew. Chem. Int. Ed.* **2005**, *44*, 3466–3470; f) X. Yang, J. Zhuang, X. Li, D. Chen, G. Ouyang, Z. Mao, Y. Han, Z. He, C. Liang, M. Wu, J. C. Yu, *ACS Nano* **2009**, *3*, 1212–1218.
- a) M. Lazzeri, A. Vittadini, A. Selloni, *Phys. Rev. B* **2001**, *63*, 155409; b) X.-Q. Gong, A. Selloni, *J. Phys. Chem. B* **2005**, *109*, 19560–19562; c) H. G. Yang, C. H. Sun, S. Z. Qiao, J. Zou, G. Liu, S. C. Smith, H. M. Cheng, G. Q. Lu, *Nature* **2008**, *453*, 638–641; d) J. Pan, G. Liu, G. Q. Lu, H.-M. Cheng, *Angew. Chem. Int. Ed.* **2011**, *50*, 2133–2137; e) Y.-F. Li, Z.-P. Liu, L. Liu, W. Gao, *J. Am. Chem. Soc.* **2010**, *132*, 13008–13015.
- a) H. G. Yang, G. Liu, S. Z. Qiao, C. H. Sun, Y. G. Jin, S. C. Smith, J. Zou, H. M. Cheng, G. Q. Lu, *J. Am. Chem. Soc.* **2009**, *131*, 4078–4083; b) G. Liu, H. G. Yang, X. Wang, L. Cheng, J. Pan, G. Q. Lu, H.-M. Cheng, *J. Am. Chem. Soc.* **2009**, *131*, 12868–12869; c) X. Han, Q. Kuang, M. Jin, Z. Xie, L. Zheng, *J. Am. Chem. Soc.* **2009**, *131*, 3152–3153; d) M. Liu, L. Piao, W. Lu, S. Ju, L. Zhao, C. Zhou, H. Li, W. Wang, *Nanoscale* **2010**, *2*, 1115–1117; e) J. S. Chen, Y. L. Tan, C. M. Li, Y. L. Cheah, D. Luan, S. Madhavi, F. Y. C. Boey, L. A. Archer, X. W. Lou, *J. Am. Chem. Soc.* **2010**, *132*, 6124–6130; f) S. Liu, J. Yu, M. Jaroniec, *J. Am. Chem. Soc.* **2010**, *132*, 11914–11916.
- a) C. Z. Wen, H. B. Jiang, S. Z. Qiao, H. G. Yang, G. Q. Lu, *J. Mater. Chem.* **2011**, *21*, 7052–7061; b) S. Liu, J. Yu, M. Jaroniec, *Chem. Mater.* **2011**, *23*, 4085–4093; c) H. Zhang, P. Liu, F. Li, H. Liu, Y. Wang, S. Zhang, M. Guo, H. Cheng, H. Zhao, *Chem. Eur. J.* **2011**,

- 17, 5949–5957; d) H. Zhang, Y. Han, X. Liu, P. Liu, H. Yu, S. Zhang, X. Yao, H. Zhao, *Chem. Commun.* **2010**, 46, 8395–8397.
- [6] M. Liu, L. Piao, L. Zhao, S. Ju, Z. Yan, T. He, C. Zhou, W. Wang, *Chem. Commun.* **2010**, 46, 1664–1666.
- [7] a) Q. Xiang, J. Yu, M. Jaroniec, *Chem. Commun.* **2011**, 47, 4532–4534; b) W. Yang, J. Li, Y. Wang, F. Zhu, W. Shi, F. Wan, D. Xu, *Chem. Commun.* **2011**, 47, 1809–1811.
- [8] C. Z. Wen, J. Z. Zhou, H. B. Jiang, Q. H. Hu, S. Z. Qiao, H. G. Yang, *Chem. Commun.* **2011**, 47, 4400–4402.
- [9] a) H. Zhang, Y. Wang, P. Liu, Y. Han, X. Yao, J. Zou, H. Cheng, H. Zhao, *ACS Appl. Mater. Interfaces* **2011**, 3, 2472–2478; b) Y. Wang, H. Zhang, Y. Han, P. Liu, X. Yao, H. Zhao, *Chem. Commun.* **2011**, 47, 2829–2831; c) T. Taguchi, Y. Saito, K. Sarukawa, T. Ohno, M. Matsumura, *New J. Chem.* **2003**, 27, 1304–1306.
- [10] P. Liu, H. Zhang, H. Liu, Y. Wang, X. Yao, G. Zhu, S. Zhang, H. Zhao, *J. Am. Chem. Soc.* **2011**, 133, 19032–19035.
- [11] J. K. Burdett, T. Hughbanks, G. J. Miller, J. W. Richardson, J. V. Smith, *J. Am. Chem. Soc.* **1987**, 109, 3639–3646.
- [12] a) N. M. Laptash, I. G. Maslennikova, T. A. Kaidalova, *J. Fluorine Chem.* **1999**, 99, 133–137; b) M. Estruga, M. Casas-Cabanas, D. Gutiérrez-Tauste, C. Domingo, J. A. Ayllón, *Mater. Chem. Phys.* **2010**, 124, 904–907.
- [13] a) D. Li, H. Haneda, N. K. Labhsetwar, S. Hishita, N. Ohashi, *Chem. Phys. Lett.* **2005**, 401, 579–584; b) D. Li, H. Haneda, S. Hishita, N. Ohashi, *Chem. Mater.* **2005**, 17, 2588–2595; c) H. Park, W. Choi, *J. Phys. Chem. B* **2004**, 108, 4086–4093.
- [14] J. C. Yu, J. Yu, W. Ho, Z. Jiang, L. Zhang, *Chem. Mater.* **2002**, 14, 3808–3816.
- [15] a) M. E. Levin, M. Salmeron, A. T. Bell, G. A. Somorjai, *Surf. Sci.* **1988**, 195, 429–442; b) N. Sakai, R. Wang, A. Fujishima, T. Watanabe, K. Hashimoto, *Langmuir* **1998**, 14, 5918–5920.
- [16] A. Turković, D. Šokčević, *Appl. Surf. Sci.* **1993**, 68, 477–479.
- [17] a) S. Milicev, J. Macek, *J. Chem. Soc. Dalton Trans.* **1984**, 297–299; b) A. P. Lane, D. W. A. Sharp, *J. Chem. Soc. A* **1969**, 2942–2945; c) P. A. W. Dean, D. F. Evans, *J. Chem. Soc. A* **1967**, 698–701.
- [18] K. Wiegardt, U. Quilitzsch, J. Weiss, B. Nuber, *Inorg. Chem.* **1980**, 19, 2514–2519.
- [19] T. Ohsaka, F. Izumi, Y. Fujiki, *J. Raman Spectrosc.* **1978**, 7, 321–324.
- [20] a) R. A. Nyquist, R. O. Kagel, *Infrared Spectra of Inorganic Compounds (3800–45 cm⁻¹)*, Academic Press, New York, **1971**; b) I. R. Beattie, T. R. Gilson, *J. Chem. Soc. A* **1969**, 2322–2327.
- [21] a) C. Z. Wen, Q. H. Hu, Y. N. Guo, X. Q. Gong, S. Z. Qiao, H. G. Yang, *Chem. Commun.* **2011**, 47, 6138–6140; b) J. Zhu, D. Zhang, Z. Bian, G. Li, Y. Huo, Y. Lu, H. Li, *Chem. Commun.* **2009**, 5394–5396; c) S. Xie, X. Han, Q. Kuang, J. Fu, L. Zhang, Z. Xie, L. Zheng, *Chem. Commun.* **2011**, 47, 6722–6724; d) J. C. Lytle, H. Yan, R. T. Turgeon, A. Stein, *Chem. Mater.* **2004**, 16, 3829–3837.
- [22] a) H. Zhao, D. Jiang, S. Zhang, W. Wen, *J. Catal.* **2007**, 250, 102–109; b) H. Zhao, D. Jiang, S. Zhang, K. Catterall, R. John, *Anal. Chem.* **2003**, 76, 155–160; c) D. Jiang, S. Zhang, H. Zhao, *Environ. Sci. Technol.* **2006**, 41, 303–308; d) S. Zhang, L. Li, H. Zhao, *Environ. Sci. Technol.* **2009**, 43, 7810–7815.
- [23] H. Zhang, P. Liu, X. Liu, S. Zhang, X. Yao, T. An, R. Amal, H. Zhao, *Langmuir* **2010**, 26, 11226–11232.
- [24] a) G. Kresse, J. Furthmüller, *Comput. Mater. Sci.* **1996**, 6, 15–50; b) G. Kresse, J. Hafner, *Phys. Rev. B* **1993**, 47, RC558; c) G. Kresse, D. Joubert, *Phys. Rev. B* **1999**, 59, 1758.
- [25] J. P. Perdew, Y. Wang, *Phys. Rev. B* **1992**, 45, 13244–13249.
- [26] D. Jiang, H. Zhao, S. Zhang, R. John, *J. Phys. Chem. B* **2003**, 107, 12774–12780.

Received: May 4, 2012
Revised: June 20, 2012
Published online:

NANO MICRO
small

Supporting Information

for *Small*, DOI: 10.1002/smll.201200971

Vapor-Phase Hydrothermal Transformation of HTiOF₃
Intermediates into {001} Faceted Anatase Single-Crystalline
Nanosheets

*Porun Liu, Yun Wang, Haimin Zhang, Taicheng An, Huagui
Yang, Zhiyong Tang, Weiping Cai, and Huijun Zhao**

Supporting Information

DOI: 10.1002/sml.201200971

Vapor-Phase Hydrothermal Transformation of HTiOF₃ Intermediates into {001} Faceted Anatase Single Crystalline Nanosheets

*Porun Liu, Yun Wang, Haimin Zhang, Taicheng An, Huagui Yang, Zhiyong Tang, Weiping Cai, Huijun Zhao**

[*] Dr. P. R. Liu, Dr. Y. Wang, Dr. H. M. Zhang, Prof. H. J. Zhao

Centre for Clean Environment and Energy

Griffith School of Environment

Griffith University

Queensland 4222 (Australia)

E-mail: h.zhao@griffith.edu.au

Prof. T. C. An

State Key Laboratory of Organic Geochemistry

Guangdong Key Laboratory of Environmental Resources Utilization and Protection

Guangzhou Institute of Geochemistry, Chinese Academy of Sciences

Guangzhou 510640 (P. R. China)

Prof. H. G. Yang

Key Laboratory for Ultrafine Materials of Ministry of Education

School of Materials Science and Engineering

East China University of Science and Technology

Shanghai 200237 (P. R. China)

Prof. Z. Y. Tang

National Centre for Nanoscience and Technology

Beijing 100190 (P. R. China)

Prof. W. P. Cai

Key Laboratory of Materials Physics

Hefei Key Laboratory of Nanomaterials and Nanotechnology

Institutes of Solid State Physics, Chinese Academy of Sciences

Hefei 230031 (P. R. China)

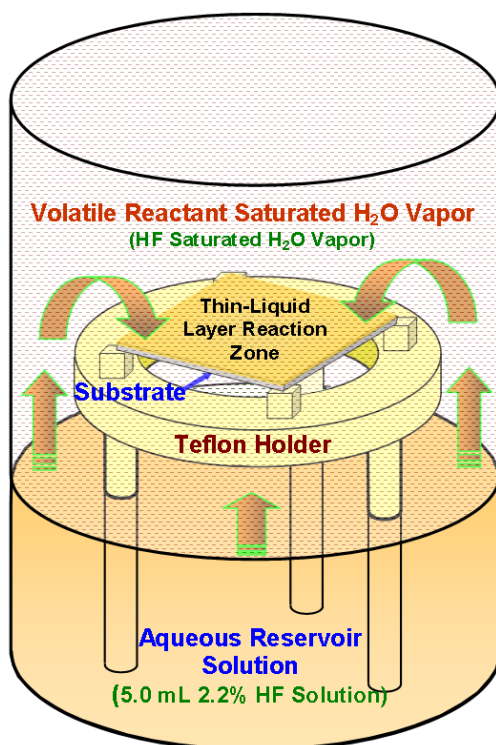


Figure S1. HF-VPH experimental set up.

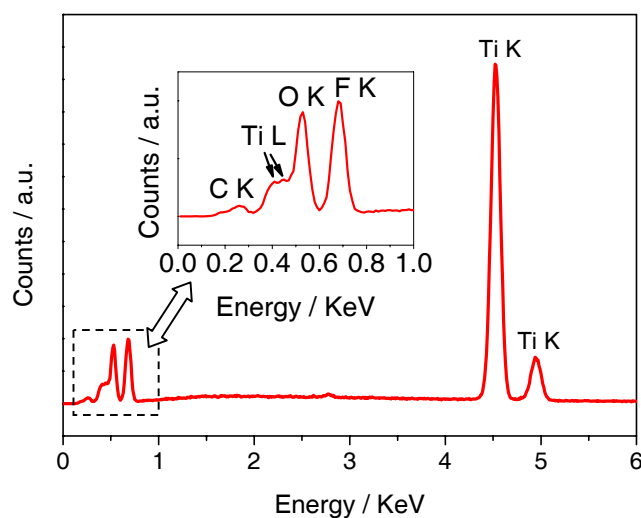


Figure S2. EDXS spectra of the intermediate (1.5 h of HF-VPH treated sample).

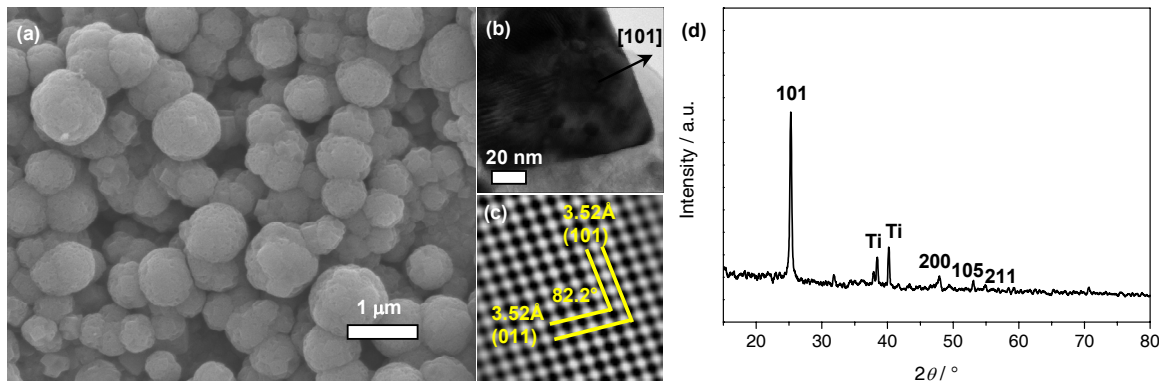


Figure S3. (a) SEM image, (b) TEM image, (c) HRTEM image and (d) XRD pattern of the sample prepared under water-VPH conditions using HTiOF_3 as the starting material at 230°C .

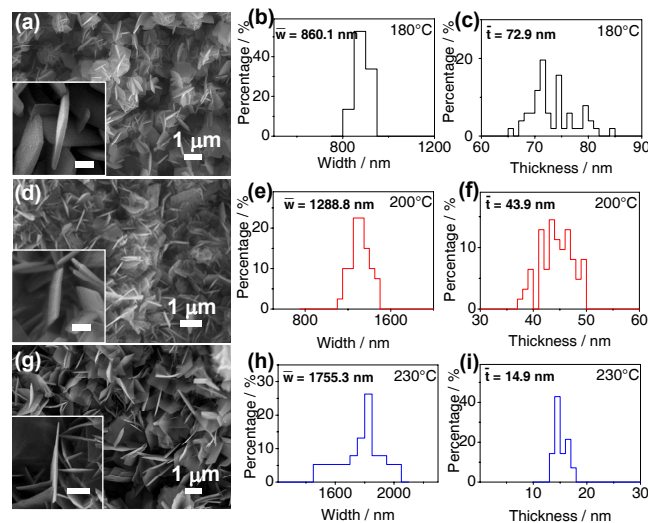


Figure S4. SEM images and dimensional properties of the nanosheets prepared by HF-VPH method at (a–c) 180°C , (d–f) 200°C and (g–i) 230°C . The scale bars in the insets of a, d, g are 400 nm.

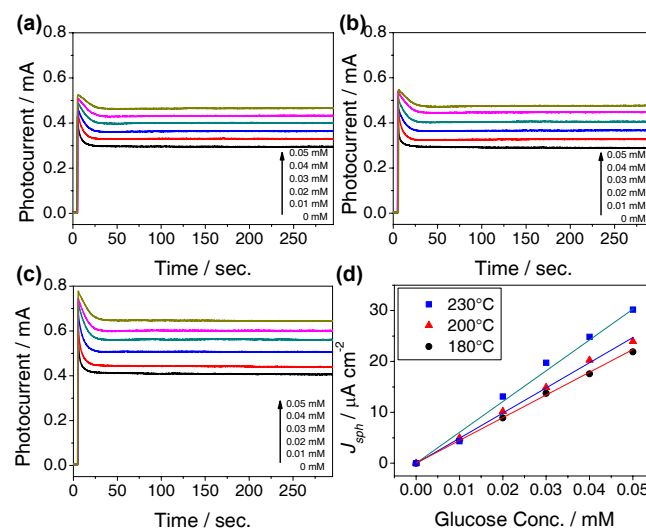


Figure S5. Photocurrent response of the $\{001\}$ faceted anatase nanosheet photoanodes prepared at different temperatures in differently concentrated glucose solutions (0 – 0.05 mM). (a) 180°C , (b) 200°C and (c) 230°C . (d) Plots of the net photocurrent density (J_{net}) in (a – c) versus the concentration of glucose.

Table S1. Comparison of the XRD data of the HTiOF₃ crystals obtained by XRD analysis and theoretical calculation.

d_{exp} [Å]	$2\theta_{\text{exp}}$ [°]	d_{cal} [Å]	$2\theta_{\text{cal}}$ [°]	h	k	l
14.020	6.312	14.055	6.296	0	0	2
23.741	3.745	23.691	3.752	1	0	0
27.602	3.229	27.652	3.223	1	0	2
28.081	3.175	28.328	3.148	0	0	4
34.142	2.6249	33.753	2.653	1	1	0
37.043	2.425	37.253	2.412	1	0	4
42.638	2.119	43.067	2.099	0	0	6
43.764	2.067	44.627	2.029	1	1	4
48.401	1.879	48.479	1.876	2	0	0
49.503	1.840	49.738	1.832	1	0	6
50.620	1.802	50.732	1.798	2	0	2
54.799	1.674	54.647	1.678	1	2	0
55.617	1.651	55.806	1.646	1	1	6
56.859	1.618	56.724	1.622	2	1	2
57.800	1.594	57.103	1.612	0	2	4
59.362	1.556	58.601	1.574	0	0	8
63.024	1.474	62.687	1.481	1	2	4
66.366	1.407	66.831	1.399	2	0	6
68.825	1.363	69.364	1.354	1	1	8
70.758	1.330	70.987	1.327	2	2	0
71.641	1.316	71.991	1.310	1	2	6
76.301	1.2470	76.025	1.2508	3	0	0
77.441	1.2314	77.786	1.2268	0	3	2
78.600	1.2161	78.110	1.2226	2	2	4